Modulation of Mo-Fe-C sites over mesoscale diffusion-enhanced hollow sub-micro reactors toward boosted electrochemical water oxidation

Feilong Gong
Zhengzhou University of Light Industry
Mengmeng Liu
Zhengzhou University of Light Industry
Lihua Gong
Zhengzhou University of Light Industry
Sheng Ye
Dalian Institute of Chemical Physics, CAS
Qike Jiang
Dalian Institute of Chemical Physics
Guang Zeng
Dalian Institute of Chemical Physics, CAS
Xiaoli Zhang
Zhengzhou University
Zhikun Peng
Zhengzhou University
Yonghui Zhang
Zhengzhou University of Light Industry
Shaoming Fang
Zhengzhou University of Light Industry
Jian Liu (jian.liu@surrey.ac.uk)
University of Surrey https://orcid.org/0000-0002-5114-0404

Article

Keywords: Sub-micro reactor, MoS2, single-atom catalysts, diffusion enhancement, electrochemical water oxidation

Posted Date: November 17th, 2021

DOI: https://doi.org/10.21203/rs.3.rs-1072780/v1

Version of Record: A version of this preprint was published at Advanced Functional Materials on April 12th, 2022. See the published version at https://doi.org/10.1002/adfm.202202141.

Modulation of Mo-Fe-C sites over mesoscale diffusion-enhanced hollow sub-micro reactors toward boosted electrochemical water oxidation

Feilong Gong[1,6], Mengmeng Liu[1,6], Lihua Gong[1], Sheng Ye[2,4*], Qike Jiang[2], Guang Zeng[2], Xiaoli Zhang[5], Zhikun Peng[5], Yonghui Zhang[1], Shaoming Fang[1*], Jian Liu[2,3*]

[1]Key Laboratory of Surface and Interface Science and Technology of Henan Province, College of Material and Chemical Engineering, Zhengzhou University of Light Industry, Zhengzhou, Henan, 450001, China

[2]State Key Laboratory of Catalysis, Dalian Institute of Chemical Physics, Chinese Academy of Sciences, Dalian, Liaoning, 116023, China

[3]DICP-Surrey Joint Centre for Future Materials, Department of Chemical and Process Engineering and Advanced Technology Institute of University of Surrey, Guildford, Surrey, GU2 7XH, UK

[4]Department of Applied Chemistry, Anhui Agricultural University, Hefei 230036, PR China

[5]Henan Institutes of Advanced Technology, State Centre for International Cooperation on Designer Low-Carbon & Environmental Materials, School of Materials Science and Engineering, Zhengzhou University, Zhengzhou 450001, China

E-mail: jian.liu@surrey.ac.uk, jianliu@dicp.ac.cn

[6]These authors contributed equally. Feilong Gong, Mengmeng Liu.

Keywords: Sub-micro reactor; MoS_2; single-atom catalysts; diffusion enhancement; electrochemical water oxidation

Abstract

Simultaneously engineering the mesoscale mass transfer and surface reactions on the electrode can promote the kinetics of oxygen evolution reaction (OER). Herein, we report the simultaneously modulation of the mesoscale diffusion and Mo-Fe-C sites formation over monodispersed hollow Fe@MoS_2-C sub-micro reactors for boosted OER performance. According to finite element simulation and analysis, the hollow nanostructured MoS_2-C host possessed much better mesoscale diffusion properties than its solid and yolk–shell counterparts. Notably, the sulfur vacancies and intercalated carbon in the sub-micro reactor offered a unique microenvironment for Fe anchoring on Mo-Fe-C sites. The stability and activity of the sites were revealed by theoretical calculations. The resultant Fe@MoS_2-C presented an OER overpotential of 194 mV, which is much better than those of the Fe-based single-atom catalysts reported to data. Our monodispersed sub-micro reactor combined the advantage of mesoscale diffusion and single-atom sites, and it may have broad prospects for complex electrocatalytic reactions.

Introduction

Electrochemical refinement technologies, including carbon dioxide/nitrogen/oxygen reduction reaction processes, water splitting systems, and metal–air batteries are sustainable means for realizing the carbon neutrality[1-4]. As one of the key half-reactions in the electrocatalytic process, the electrochemical oxygen evolution reaction (OER) has more prospective applications than other anodic reactions[5]. However, the kinetic process of the OER is always sluggish due to the high energy barriers involving in the multi-step electrochemical water oxidation process[6],

thereby hindering catalytic efficiency. Though noble metal-based materials, such as IrO_2 and RuO_2, are their state-of-the-art catalysts for electrochemical water oxidation, the scarcity, high cost, and inferior stability have limited their widespread application in the alkaline electrolysis field[7-9]. Therefore, the design of highly active non-precious-metal OER electrocatalysts with long-term-durability is important, but remains highly challenging[5, 10, 11].

Optimizing the mass transfer behaviors of chemical species and the surface reactions over electrodes to develop highly efficient electrocatalysts is crucial for facilitating the electrochemical OER kinetics process[12-15]. In fact, considerable efforts have been devoted to the engineering of electrodes to tailor the diffusion behavior, and sufficiently rapid macroscale electrolyte transfer to electrodes has been achieved[16-18]. However, for the water-splitting reaction at the gas–liquid–solid triple-phase interface, optimizing the electrocatalysts at the mesoscale could maximize their utilization, which is an important strategy for promoting the catalytic process[19]. Two-dimensional (2D) layered molybdenum sulfide (MoS_2) has potential electrocatalytic application[20, 21], while its 2D configuration could be easily self-stacked leading to disillusionary mass transfer property[22, 23]. As a result, mass diffusion could become the determining factor of the electrocatalytic process. For this reason, it is of great significance for the innovative design of the geometric configurations of MoS_2 materials to optimize mass diffusion at the mesoscale. For example, benefitting from the three-dimensional (3D) hierarchical nanoarchitectures[24-26] self-assembled by 2D nanosheets, the mass transfer properties of electrodes could be enhanced to some extent. The design of nanoarrays could provide a shorter electron or ion transfer path and increase the accessibility of catalytic sites[27, 28]. Meanwhile, 3D ordered channels are available for electrolyte diffusion, thereby enhancing electrocatalysis[12, 29]. Notably,

multilevel nanostructured materials with porous shell layers and inner spaces can yield catalysts that can be readily infiltrated by electrolytes, with rich paths for mass diffusion[30-34].

In addition, the improvement of the surface reactions on the electrode has focused on regulating the active sites of the catalysts[35-37]. Single-atom site catalysts (SACs) possess 100% atomic utilization efficiency, quantum size effects, and highly tunable electronic states, endowing the materials with superb electrocatalytic properties[38-40]. The interactions between the support and the metal, which are closely related to the coordination environment, could play a key role for the activity, durability, and selectivity of electrocatalysts[41-43]. Therefore, the support could have a noticeable impact on the efficiency of SACs. Over the past decade, the structure–property relationships of carbon-supported SACs with unsaturated, saturated, and super saturated coordination environments have been systematically studied[44-48]. Recently, non-carbon supports such as metal oxides, metal chalcogenides, and metal hydroxides, have demonstrated potentially for the construction of SACs than carbon supports[49-51]. Because of the multifarious anchoring mechanisms[52, 53], it may be more profitable to maximize the atomic utilization and stability of SACs in non-carbon hosts. According to previous research, engineering MoS_2-based materials via self-tailoring[54, 55], doping[56, 57], and interface formation[58, 59] can create abundant sites, which could possibly be used for anchoring metal atoms. Importantly, it is feasible to simultaneously obtain pre-eminent electronic structures and mass transfer properties via the engineering of nanoreactors[60-62]. Inspired by this, the modulation of single-atom catalytic sites on mesoscale diffusion-enhanced MoS_2-based material platforms to design sub-micro reactors could be of great importance for boosting electrochemical water oxidation.

In this study, we reported the simultaneously modulation of the mesoscale diffusion and Mo-Fe-C active site formation over monodispersed hollow Fe@MoS_2-C sub-micro reactors for highly efficient electrochemical water oxidation. A group of MoS_2-C hosts assembled by carbon-intercalated MoS_2 nanosheets were prepared through a micelle-confined microemulsion technology. According to finite element simulation and analysis (FEA), the hollow nanostructured configuration possessed much better mesoscale mass transfer properties than solid and yolk–shell structures. The monodispersed hollow MoS_2-C host with a dual coordination environment for Fe anchoring was used to develop the Fe@MoS_2-C sub-sub-micromicro reactor. The resultant catalyst exhibited a significantly lower OER overpotential than those of Fe-based SACs reported so far, and it also exhibited superior durability. Density functional theory (DFT) revealed the high activity and stability of the Mo-Fe-C sites.

Results

Structural characterization, FEA, and OER assessment of MoS_2-C. Three kinds of monodispersed MoS_2-C materials were successfully synthesized by a micelle-confined microemulsion technology (Supplementary Fig. 1). The configurations of the materials can be changed dramatically from solid to yolk–shell to hollow spheres. Specifically, the solid spheres with diameters of *ca.* 540 nm were assembled from nanosheets by adding 1.2 mL hydrochloric acid (Fig. 1a, Supplementary Figs. 1a and 2). The spheres were converted to yolk–shell configurations after regulating the amount of hydrochloric acid to between 0.8 and 0.6 mL. The diameter and the wall thickness of the yolk–shell sphere (*ca.* 650 nm) remained unchanged, while the core gradually decreased with the decline in the hydrochloric acid (Fig. 1b, Supplementary Figs. 1b−d and 3). By reducing the amount of hydrochloric acid to 0.5–0.3 mL, the monodispersed and uniform hollow spheres with diameters of *ca.* 750 nm could be

prepared (Fig. 1b, Supplementary Figs. 1e−g and 4). As indicated by the transmission electron microscopy (TEM) results, the wall thicknesses of the spheres were *ca.* 20, 40, and 75 nm for the hollow MoS_2-C-1, MoS_2-C, and MoS_2-C-3, respectively.

According to the X-ray diffraction (XRD) profiles, the main peaks of the as-prepared materials could be attributed to 2H-MoS_2 (JCPDS 37–1492). Interestingly, a (002) peak of the MoS_2 at 14.2° was not found, while a new peak at 9.4° corresponding to a lattice spacing of 0.96 nm appeared, demonstrating the intercalation of monomolecular carbon[63]. Based on Fourier-transform infrared spectroscopy (FT-IR), the carbon intercalation could be derived from the graphitization of cetrimonium bromide (CTAB, Supplementary Fig. 6). The specific surface areas were 41.2, 59.1, and 90.7 $m^2\ g^{-1}$ for the solid, yolk-shell, and hollow MoS_2-C, respectively, and mesopores were present, supplying rich diffusion channels (Supplementary Fig. 7a–c). The average pore sizes were 13.1, 16.2, and 21.0 nm for the solid, yolk–shell, and hollow MoS_2-C, respectively (Supplementary Fig. 7d).

FEA was conducted to investigate the mass transfer properties at the mesoscale and to obtain a better understanding of the superiority of the engineered MoS_2-C hosts. Based on the experimental characterization, the models were correspondingly constructed for solid, yolk–shell, and hollow nanostructured MoS_2-C materials. Diagrams of the models are shown in Supplementary Fig. 8a−c. The simulated velocity fields are shown in Fig. 1d−1f, and the corresponding flow velocity at the outer boundary (path 1) and mid-position (path 2) is shown in Supplementary Fig. 8d−i. The flow rate of the fluid was greatly influenced by the geometric configurations of the materials. As shown from the simulated results of path 1, the flow rate in the hollow sphere was much larger than those in the solid and yolk–shell spheres, except that very few positions were approximately equal to those of the yolk–

shell spheres. More importantly, the hollow model had a clear advantage in terms of the flow velocity over the solid and yolk–shell spheres for path 2. The pressure distribution of the material in the fluid was another important index to evaluate the mesoscale mass diffusion. As shown by the comparison of the pressure fields (Fig. 1g–i), a significant pressure difference was generated between the outside and inside in the hollow-structured model. In contrast, the pressure difference became weaker in the solid and yolk–shell models. In general, the higher flow velocity and pressure difference in the hollow-nanostructured catalyst could be conducive to the full and rapid contact between the electrode and electrolyte, thereby promoting the mass transfer of the electrolyte at the mesoscale.

The static contact angles (CAs) are 61.9° and 57° for the solid and yolk–shell MoS_2-C, respectively (Supplementary Fig. 9). In contrast, the CA of the hollow spheres decreased to 42.6°. The enhanced hydrophilicity may have been due to the vertical self-assembly of the layer-expanded nanosheets onto the hollow spheres. There was no doubt that the higher surface wettability of the hollow-structured catalyst would ensure fast electrolyte penetration and accelerate the migration of hydroxyl groups. Next, we studied the electrochemical water oxidation performances of the as-prepared materials to reveal the structure–property relationships. In contrast, the hollow MoS_2-C catalyst with optimal mesoscale diffusion properties delivered an overpotential of 303 mV (10 mA cm^{-2}) and a Tafel slope of 79 mV, which was better than those of the hollow MoS_2-C-1, hollow MoS_2-C-3, solid MoS_2-C, and yolk–shell MoS_2-C catalysts (Fig. 1j and Supplementary Fig. 10). This result indicated that the mesoscale diffusion of the electrolyte could be highly enhanced via the engineering of the microstructure of the catalyst, thus promoting the catalytic process. Nonetheless, the OER activity of the hollow MoS_2-C was still inferior to those of the catalysts

reported to data (Supplementary Table 3) because of the simple and scanty active sites.

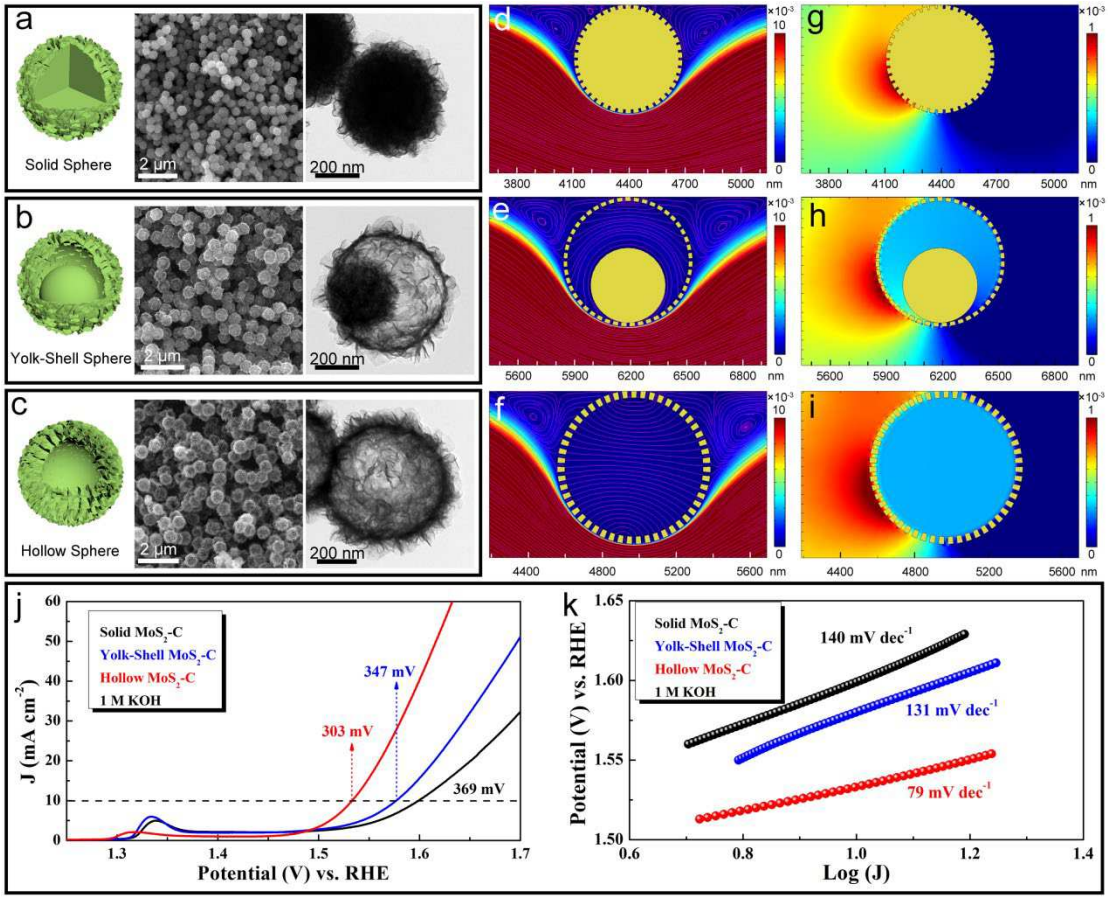

Fig. 1 Structural information, and FEA results, and OER activities of MoS_2-C materials. FESEM and TEM images of **a** solid MoS_2-C, **b** yolk–shell MoS_2-C, and **c** hollow MoS_2-C. **d**–**f** Velocity fields, streamline distributions, and **g**–**i** pressure fields of different nanostructured models. **j** Polarization curves and **k** Tafel slopes of solid, yolk–shell, and hollow MoS_2-C catalysts.

Preparation and characterization of monodispersed hollow sub-micro reactors. To further improve the OER performance, a series of monodispersed sub-micro reactors were designed via the elaborate functionalization of the hollow MoS_2-C. The carbon-intercalated MoS_2-C host was first prepared by the treatment of the hollow precursor, which was subsequently thoroughly mixed with Fe^{3+}. The resultant powder was treated via a calcination process to obtain the monodispersed Fe@MoS_2-C sub-

micro reactor (Fig. 2a and Supplementary Fig. 11). According to the XRD profiles (Supplementary Fig. 12), the corresponding lattice distance of the (002) facet was reduced from 1.1 nm for MoS_2-CTAB to 0.96 nm for MoS_2-C and Fe@MoS_2-C, and it was further decreased to a typical value of 0.62 nm for Fe@MoS_2 and MoS_2.

As shown by the field-emission scanning electron microscope (FESEM) images, the MoS_2-CTAB precursor exhibited a monodispersed feature with a diameter of *ca.* 840 nm, and the nanosheets were vertically assembled onto the well-defined spheres, forming a quasi-nanoarray (Supplementary Fig. 13). After the calcination, the morphology remained constant, while the size of the MoS_2-C decreased to *ca*. 750 nm. The self-assembled array on the MoS_2-C could supply rich channels for electrolyte diffusion and gas release, which was consistent with the Brunauer–Emmett–Teller (BET) and CA results (Supplementary Fig. 14). After introducing Fe, the structure, size, and nanoarray of the MoS_2-C remained unchanged, exhibiting a stable nanoarchitecture (Fig. 2b, c and Supplementary Fig. 15). Notably, the diameters of the hollow MoS_2 and Fe@MoS_2 microspheres were reduced to *ca.* 670 nm, and the vertical nanosheets tended to collapse compared with those in the MoS_2-C and Fe@MoS_2-C (Supplementary Figs. 16, 17). Significantly, the monodispersed and uniform microspheres could be controllably prepared on a large scale using the low magnification FESEM images and the size distributions (Supplementary Figs. 13–17).

TEM and high-resolution TEM (HRTEM) image images of the MoS_2-CTAB showed its hollow structure, and an expanded space was observed due to the intercalation of CTAB (Supplementary Fig. 18). The hollow nanostructured configurations remained almost constant after the heat treatment, while the expanded lattice was reduced to 0.96 nm in the MoS_2-C and to 0.62 nm in the MoS_2 (Supplementary Figs. 19–21). As shown in the high-angle annular-dark-field

(HAADF) image and the corresponding energy-dispersive X-ray spectroscopy (EDS) mappings of MoS_2-C, the elements Mo, S, and C were homogeneously distributed in the microsphere. After introducing Fe, neither the hollow nanostructures nor the expanded layer were affected (Fig. 2d, e). The aberration-corrected HAADF and corresponding annular-bright-field (ABF) images revealed that the monomolecular carbon was successfully intercalated in the (002) facet of MoS_2 to generate a superlattice (Fig. 2f, g). The low- and high-magnification HAADF images and the EDS mapping for Fe@MoS_2-C indicated that the element distribution in the nanosheet-assembled hollow sub-micro reactor was homogeneous (Fig. 2h and Supplementary Fig. 20). No aggregation was evident in the EDS mapping image of Fe. We performed the spherical aberration-corrected HAADF scanning transmission electron microscopy (HAADF-STEM) to further visually estimate the Fe distribution (Fig. 2i, j). Speckled bright dots (yellow circles) existed on the surfaces and in the interlayer, demonstrating that single-atom Fe was atomically isolated in the sub-micro reactor. The Raman spectra of MoS_2-C and Fe@MoS_2-C (Supplementary Fig. 22) displayed typical vibration peaks of 2H-MoS_2 and defective carbon. In contrast, both the out-of-plane A_{1g} and in-plane E^1_{2g} vibrations of Mo-S were blue-shifted in the Fe@MoS_2-C further confirming the interaction between MoS_2 and single-atom Fe.

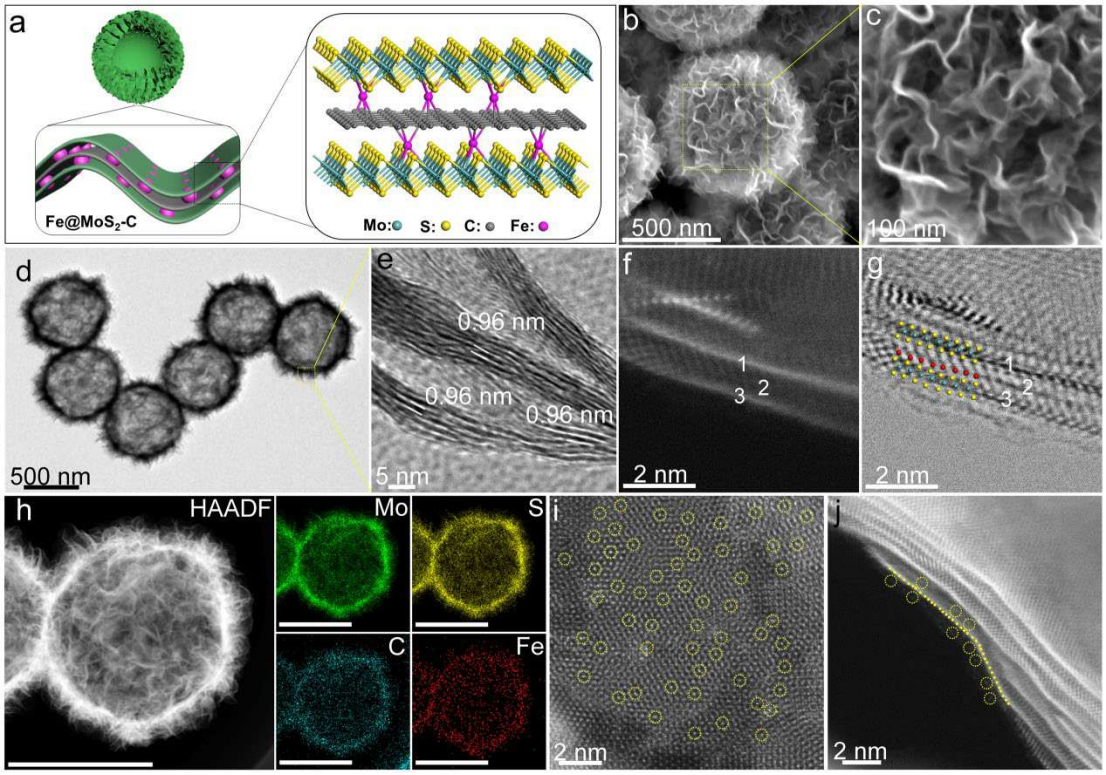

Fig. 2 Structural characterization of hollow Fe@MoS_2-C sub-micro reactor. a Schematic diagram and crystal structure, **b, c** FESEM images, **d** TEM image, and **e** HRTEM image. **f** HAADF image with **g** corresponding ABF image, **h** HAADF image, EDS mapping, and HAADF-STEM images **i** on the surface and **j** at the edge.

Electron paramagnetic resonance (EPR) was carried out to study the sulfur vacancies before and after carbon intercalation. Compared with MoS_2, MoS_2-C delivered larger signal at ~3484 G (Supplementary Fig. 23), indicating that introducing monolayer carbon in the interlayer could lead to the enhancement of the sulfur vacancies. The correlation between Fe and the MoS_2-C host was revealed by X-ray photoelectron spectroscopy (XPS). According to the comparison of the Mo 3d spectra, a pair of peaks at 229.0 and 232.2 eV attributed to Mo^{4+} were fitted, and they were positively shifted by 0.3 eV after introducing Fe (Fig. 3a). Meanwhile, the binding energies of S 2p (163.1 and 162.0 eV) also increased by 0.2 eV in the Fe@MoS_2-C compared with those of the MoS_2-C (Supplementary Fig. 24b). In the

high-resolution Fe 2p spectrum of the Fe@MoS_2-C, two peaks at 712.9 and 726.0 eV belonged to the Fe 2p3/2 and Fe 2p1/2 of Fe^{3+}, respectively, and the couple peaks at 717.6 and 730.6 eV were satellite peaks (Fig. 3b). Another two weak peaks at 706.9 and 720.6 eV, which were respectively assigned as Fe^{3+} 2p3/2 and Fe^{3+} 2p1/2 of the Fe-C bonds, were also identified. A new peak at 283.7 eV was evident in the C1s spectra (Fig. 3c). The above XPS analysis indicated the strong electronic interactions between Mo and Fe as well as the formation of Fe-C bonds in the Fe@MoS_2-C. Similar peak shifts were found in the Fe@MoS_2 and MoS_2 except that the peaks associated with Fe-C disappeared (Supplementary Fig. 25). Based on the inductively coupled plasma mass spectrometry (ICP-MS) result (Supplementary Table 1), the concentrations of Fe were 54.5 and 27.5 μg L^{-1} in the Fe@MoS_2-C and Fe@MoS_2, respectively, which corresponded to 1.09 and 0.55 wt.%.

We collected the X-ray absorption near-edge structure (XANES) and extended X-ray absorption fine structure (EXAFS) of the Fe K-edge to determine the electronic states and the local structural information around the Fe in the Fe@MoS_2-C. According to the XANES spectroscopy results of the Fe K-edge (Fig. 3d), the white line intensity in the range of 7128–7136 eV was similar to that of the Fe_2O_3 reference (7132.8 eV), signifying the presence of Fe^{3+} in the Fe@MoS_2-C, which was consistent with the XPS analysis. Atomic coordination information of Fe was revealed by Fourier-transformation EXAFS spectroscopy. Compared with the radial distance space spectra χ(R) of the Fe foil and Fe_2O_3 reference, a prominent peak at *ca.* 1.69 Å belonging to the first shell of the Fe-C scattering signal was clearly identified, while no Fe-Fe signal was evident at *ca.* 2.23 Å, demonstrating the atomic dispersion of Fe in the Fe@MoS_2-C (Fig. 3e). Notably, a weak signal at *ca.* 2.64 Å assigned to the scattering signal of the Fe-Mo pair can also be found. Accordingly, the electron

transfer could be existed between Fe and Mo, which was in agreement with XPS spectra. The high-resolution wavelet-transform EXAFS was obtained to intuitively show the formation of Fe-C and Fe-Mo pairs. Specifically, the Fe@MoS_2-C delivered the highest intensity at *ca.* 1.69 Å attributed to the Fe-C pairs (Fig. 3f). To better understand the local geometry, EXAFS fitting was carried out, and the parameters and k-space are shown in Supplementary Table 2 and Fig. 26, respectively. The fit indicated that the Fe-C distance was 2.11 Å with a coordination number of around 3. In addition, a significant lobe appeared above 2 Å, which indicated that the Mo could be coordinated with metal Fe, forming the Fe-Mo pair. Based on the above detailed XAFS results, atomically dispersed Fe was anchored by the C and Mo atoms of the hollow MoS_2-C, forming a sub-micro reactor.

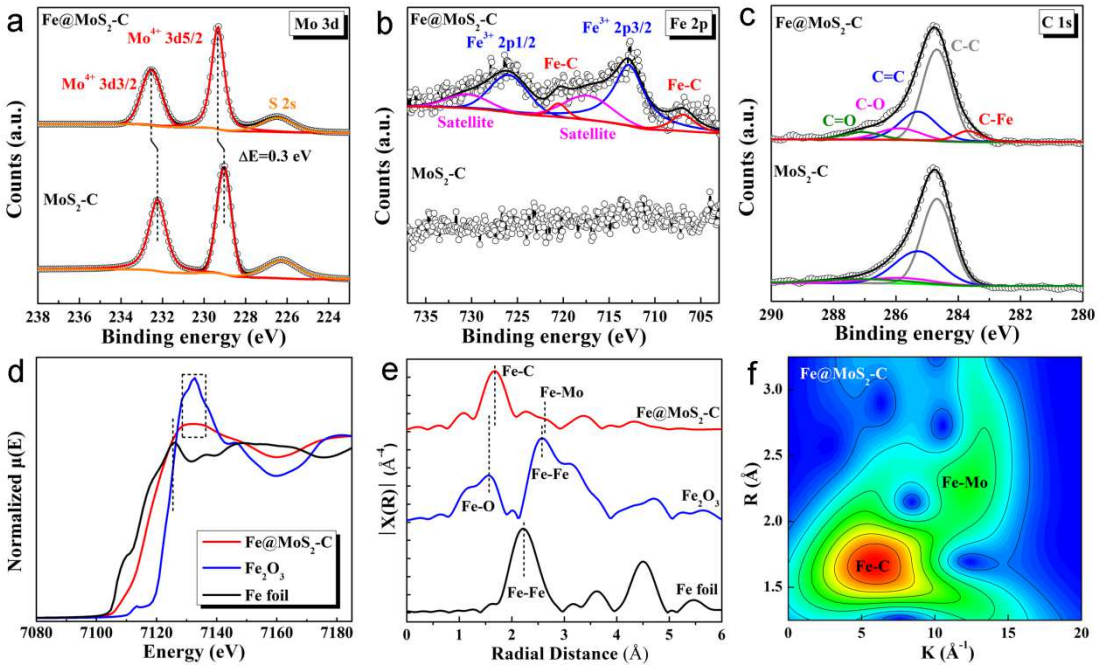

Fig. 3 Structural characterization of Mo-Fe-C site. a–c High-resolution Mo 3d, Fe 2p, and C 1s XPS spectra for the hollow MoS_2-C and Fe@MoS_2-C. **d** Fe K-edge XANES, **e** Fe K-edge EXAFS spectra, and **f** wavelet transform for Fe k^3 weighted signal of Fe@MoS_2-C.

Electrocatalytic OER evaluation. The OER performances of the as-prepared monodispersed hollow Fe@MoS_2-C, Fe@MoS_2, MoS_2-C, MoS_2, S-Fe@MoS_2-C, and Y-Fe@MoS_2-C sub-micro reactors were systematically compared, and the commercial IrO_2 was tested for comparison. As shown by the polarization curves in 1 M KOH (Fig. 4a), the Fe@MoS_2-C catalyst delivered an overpotential of 194 mV at 10 mA cm^{-2}, which was lower than those of Fe@MoS_2 (239 mV), MoS_2-C (303 mV), and MoS_2 (362 mV), exhibiting the highly improved OER activity after carbon intercalation and single-atom Fe anchoring. The corresponding Tafel slope of 63 mV dec^{-1} was also lowered for the Fe@MoS_2-C catalyst compared with those of the Fe@MoS_2, MoS_2-C, and MoS_2 (Fig. 4b). In addition, the activity of the hollow Fe@MoS_2-C catalyst for water oxidation was much higher than those of the S-Fe@MoS_2-C and Y-Fe@MoS_2-C materials based on the polarization curves and Tafel slopes (Supplementary Fig. 27), which could be attributed to the highly enhanced mesoscale mass transfer behavior in the monodispersed hollow sub-micro reactors. Importantly, the overpotential of the Fe@MoS_2-C catalyst was reduced by 138 mV compared with that of commercial IrO_2. Furthermore, the monodispersed hollow Fe@MoS_2-C sub-micro reactor exhibited the lowest OER overpotential of the Fe-based SACs reported in the literature (Fig. 4c and Supplementary Table 3).

According to the electrochemical impedance spectroscopy (EIS) curves (Supplementary Fig. 28a), the Fe@MoS_2-C catalyst exhibited the lowest charge transfer resistance, revealing the fastest charge transfer kinetics. The double-layer capacitance was 35.8 mF cm^{-2} for the Fe@MoS_2-C, which was much higher than the values of 23.0 mF cm^{-2} for the Fe@MoS_2, 8.3 mF cm^{-2} for the MoS_2-C, and 3.5 mF cm^{-2} for the MoS_2, verifying that the Fe@MoS_2-C had the highest number of active sites (Supplementary Figs. 28b and 29). As shown in the Supplementary Fig. 28c, the

turnover frequency (TOF) value of the Fe@MoS_2-C catalyst was calculated to be 17.75 s^{-1} at 300 mV, which was 38 times higher than that of MoS_2, implying that the intrinsic activity of the sites was dramatically enhanced. To further assess the durability of the Fe@MoS_2-C catalyst, we conducted electrolytic measurement using the chronoamperometric method. The overpotentials of the sub-micro reactor exhibited almost no attenuation during continuous measurements at 10, 50, 100, and 200 mA cm^{-2} (Supplementary Fig. 28d). The multistep chronoamperometric result demonstrated that the Fe@MoS_2-C catalyst could possess the superior durability and rate capabilities for electrochemical water oxidation.

Furthermore, the OER activity in a strongly alkaline environment was investigated to estimate the potential application in industrial environments. The OER activity was gradually improved in the increase of the alkaline concentration of the electrolyte, and an overpotential of 155 mV could be achieved when the alkalinity approximated to that of industrial conditions (Supplementary Fig. 30a). Accordingly, the Tafel slope was reduced to 43 mV dec^{-1} in 6 M KOH (Supplementary Fig. 30b). The stability of the Fe@MoS_2-C catalyst was studied in 6 M KOH, which exhibited slight attenuation in the electrolytic OER test for 120 h at 100 mA cm^{-2}, further revealing its excellent durability under strongly alkaline conditions (Fig. 4d).

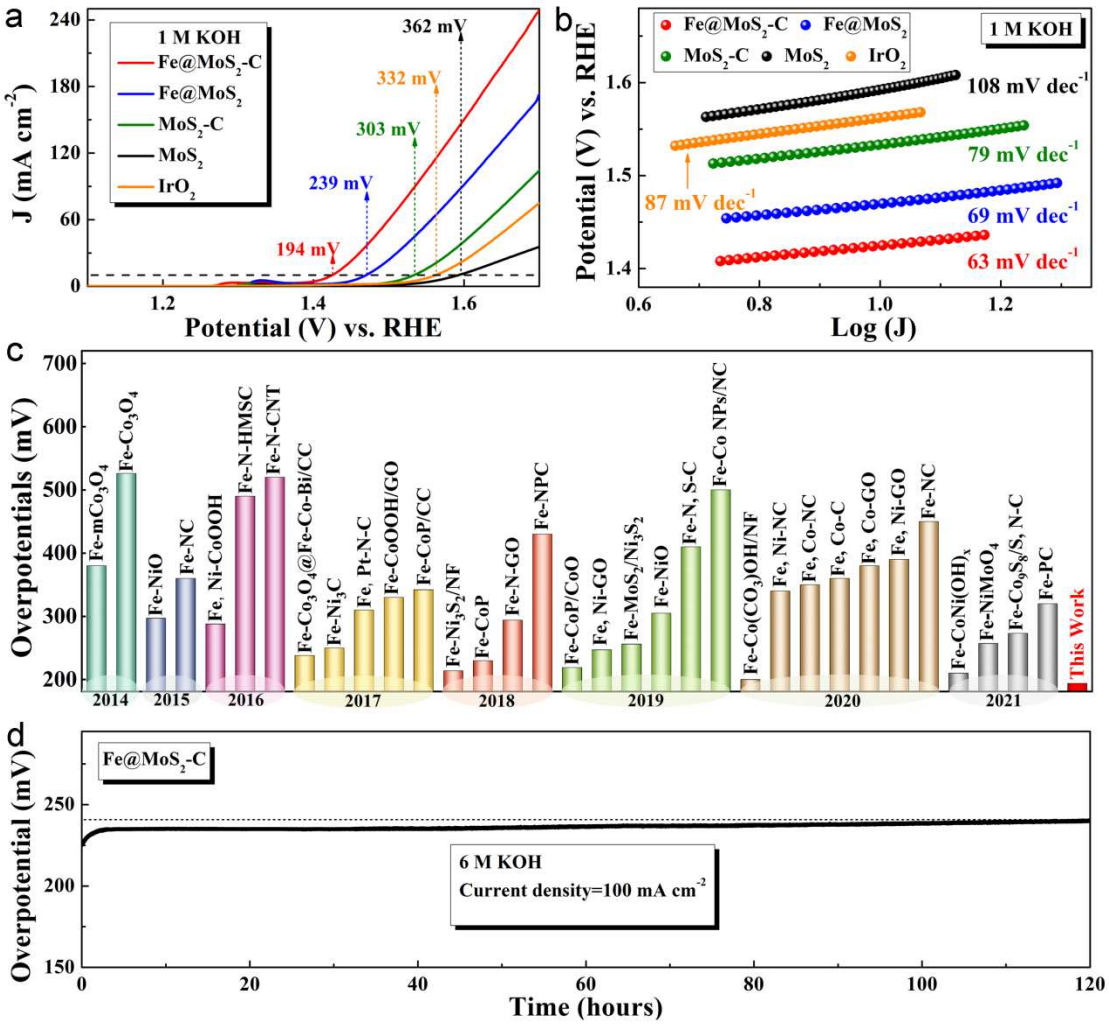

Fig. 4 OER performances of monodispersed hollow nanostructured catalysts. a Polarization curves and **b** Tafel slopes. **c** Comparison of the overpotential for the Fe@MoS2-C and reported Fe SAs. **d** Electrocatalytic stability of the Fe@MoS2-C catalyst at 100 mA cm^{-2}.

Operando Raman spectroscopy, durability of catalyst, and theoretical calculations. The operando Raman analysis of the Fe@MoS2-C electrode was conducted in 1M KOH at different voltages to investigate the structural evolution (Fig. 5a). The Raman signal revealed distinct changes during the OER test compared to that of the initial state. In contrast, two peaks at 377.9 and 401.0 cm^{-1} corresponding to the stretching vibrations of Mo-S could be clearly observed before applying a voltage, and these vibrations gradually decreased with the enhancement of the D and G bands

of carbon from 0 to 0.7 V. In particular, two weak peaks at 817.3 and 989.7 cm^{-1} corresponding to Mo-O vibrations appeared at 0.3 V, signifying that slight oxidation could occur in situ on the MoS_2 during the OER process. The Mo-O vibrations were gradually raised along with the increase in the applied voltage. The operando Raman data verified that the Fe@MoS_2-C catalyst could undergo reconstruction, forming an active oxidation layer during the OER process. According to the XPS results of the Fe@MoS_2-C after catalysis (Supplementary Fig. 30), two new peaks belonging to Mo^{6+} could be fitted in addition to the Mo^{4+} peaks in the Mo 3d spectrum (Supplementary Fig. 31b, f). Three couple peaks coupled Fe^{3+}, satellite, and Fe-C peaks were still evident in the Fe 2p spectrum, while their positions were positively shifted (Supplementary Fig. 31d). The results implied that Fe could be affected by high-valence-state Mo or adsorbed oxygen species.

We collected the XAFS of the Fe@MoS_2-C catalyst after catalysis to reveal the catalytic sites. The XANES region of Fe delivered a similar absorption edge intensity compared with that of the Fe_2O_3 reference, which confirmed the stable presence of Fe^{3+} in the catalyst (Supplementary Fig. 32a). According to the EXAFS, the primary scattering signal at 1.60 Å showed slight negative changes in intensity compared to that of the fresh catalyst, which can be explained as the co-contribution of Fe-C and Fe-O pairs (Fig. 3e). Meanwhile, the position of Fe-O for the catalyst after catalysis was lower than 1.69 Å of Fe-C for the fresh catalyst and higher than 1.55 Å of Fe-O for the Fe_2O_3 reference, which indicated that the Fe-O pair could be derived from the adsorbed water molecules or hydroxyl groups in the OER process. According to the EXAFS fitting result (Supplementary Table 4 and Supplementary Fig. 32b), the coordination numbers of Fe-C and Fe-O were around 3 and 1, respectively. Considering the closeness of the fitted Fe-C (2.08 Å) and Fe-O (2.06 Å) peaks, these

two peaks likely overlapped in the catalyst after catalysis. The signal of the Fe-Mo pair remained, while it also exhibited a marginal shift due to the formation of hexavalent Mo in the surficial reconstruction, which was in accordance with the XPS results. Furthermore, scattering signals of the Fe-O/Fe-O and Fe-Mo pairs also appeared in the wavelet transform contour plots. The above EXAFS results further revealed that the catalytic center of Fe^{3+} at the Mo-Fe-C sites could participate in the adsorption and desorption of oxygen intermediates during the catalytic OER.

The stability of the hollow sub-micro reactor was further visually confirmed by the unchanged configuration after the catalytic testing (Fig. 5d). The superlattice still existed revealing the stability of the carbon intercalation. Beyond that a thin layer with a thickness of of *ca.* 10 nm and poor crystallinity was generated outside the sphere (Fig. 5e) due to in-situ surface oxidation during the water oxidation process[64]. The HAADF image and EDS mapping revealed that Mo, S, C, and Fe were homogeneously distributed, while the O accumulated outside the sphere to some extent (Fig. 5f). The results were consistent with the operando Raman and XPS results, indicating the steadfastness of single-atom Fe and the reconstruction of MoS_2.

We employed DFT calculations to assess the electronic structures, Mo-Fe-C sites, and kinetics process (Supplementary Fig. 33). The stability of the single-atom Fe was first investigated via the calculation of the adsorption energy (E_{ads}) and the cohesive energy (E_{coh}). According to the criteria, both the E_{ads} and $E_{ads} - E_{coh}$ should be negative values for the atom to stabilize on the host[65, 66]. As a result, the calculated E_{ads} values of Fe atoms in the MoO_x and MoO_x-C were −4.16 and −4.47 eV, respectively, while the corresponding $E_{ads} - E_{coh}$ values were 0.12 and −0.19 eV (Fig. 5g). The result indicated that single-atom Fe could be stabilized in MoO_x-Fe-C when there were dual-anchoring sites of vacancies and carbon atoms.

As shown from the partial electronic density of states (PDOS), the peaks of the Fe d orbital overlapped with those of the Mo d and C p orbitals in the MoO_x-Fe-C to some extent, confirming the Mo-Fe-C sites (Supplementary Fig. 34). Furthermore, the d states of Fe dominated the PDOS near the Fermi levels in the MoO_x-Fe and MoO_x-Fe-C. The PDOS diagram (Supplementary Fig. 35) showed that the d-band center of Fe atoms in the MoO_x-Fe-C was at −1.19 eV, which was slightly upshifted compared with that of the MoO_x-Fe. Similarly, the d-band center of the Mo atoms was shifted to −1.01 eV from −3.05 eV after introducing Fe and carbon. The upshifted d-band center originating from the decrease in the antibonding electrons could promote charge transfer leading to effortless adsorption and desorption of the intermediates. The electron density difference (EDD) results showed that the electron redistribution occurred at the interface of MoO_x-Fe-C, and an enhanced electron transfer channel of 'MoO_x → Fe → carbon' had formed (Fig. 5h). The specific amounts of charge transfer were identified by population analysis (Supplementary Fig. 36).

The chemisorption models and processes were shown in Supplementary Figs. 37 and 38, and the free energy changes were calculated to investigate the kinetic barriers (Supplementary Fig. 39). As shown from the energy diagram, the formation of OOH* intermediates (step 3) was the rate-determining step (RDS) for MoO_x. The RDS had not changed while the energy barrier was reduced to 3.06 from 3.88 eV after introducing carbon intercalation. Because of the electron accumulation, the decomposition of OOH* intermediates was more difficult, and the RDS changed to the dissociation of OOH* intermediates for MoO_x-Fe (step 4). Compared with MoO_x-C, MoO_x-Fe delivered a much lower barrier of 2.50 eV, revealing that Fe was more predominant than carbon intercalation. Interestingly, benefitting from the enhanced electron channel of 'MoO_x → Fe → carbon', the dissociation of OOH* intermediates

for the MoO_x-Fe-C became more toilless than that of the MoO_x-Fe. Furthermore, the energy barrier of 1.98 eV (step 3) was the RDS for the MoO_x-Fe-C, which was the lowest compared with those of the MoO_x, MoO_x-C, and MoO_x-Fe. In general, the Mo-Fe-C sites could stabilize single-atom Fe, promote charge transfer, and regulate kinetics process, thereby leading to an enhanced electrochemical OER.

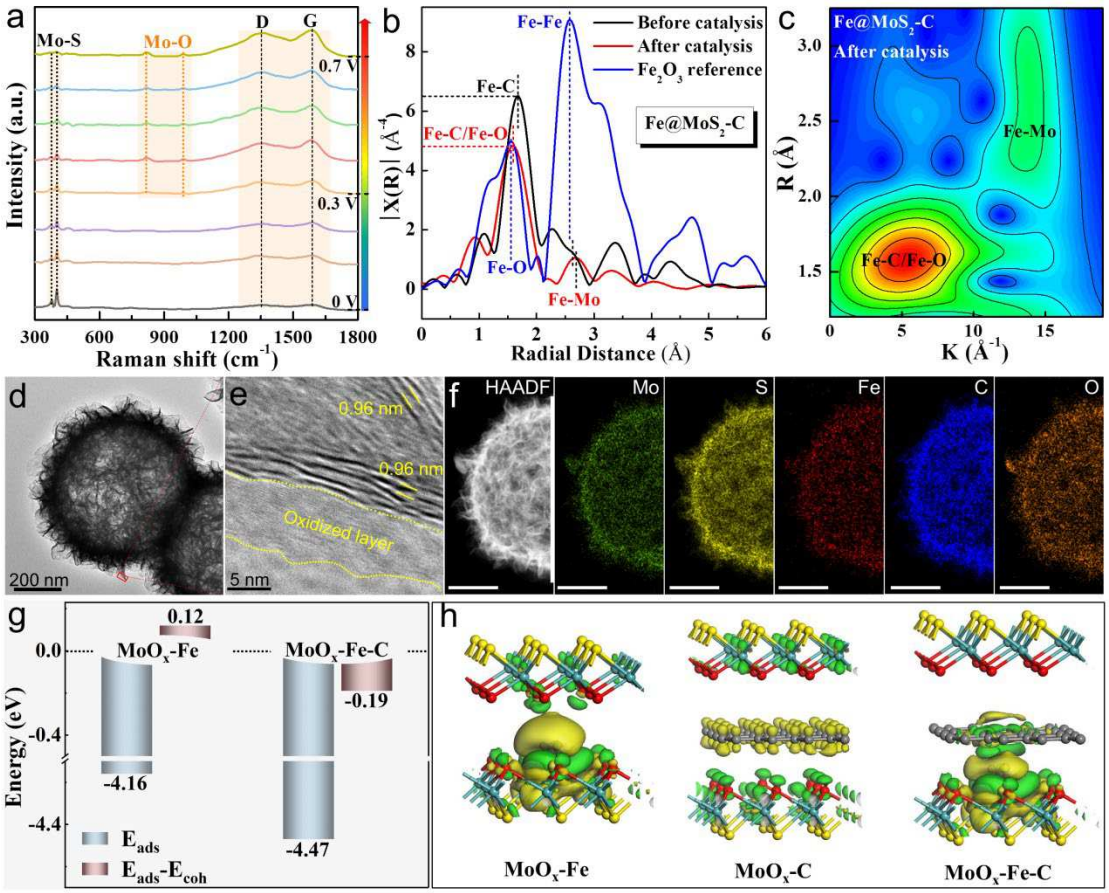

Fig. 5 Operando Raman spectra, structural characterization after catalysis, and DFT calculations. a Operando Raman, **b** Fe K-edge EXAFS spectra of the Fe_2O_3 reference and Fe@MoS_2-C, **c** wavelet transform of the Fe@MoS_2-C after catalysis, **d** TEM image, **e** HRTEM image, **f** HAADF image and corresponding EDS mapping, **g** theoretical stability of the single-atom Fe, **h** EDDs of the MoO_x-C, MoO_x-Fe, and MoO_x-Fe-C. Isovalue in **h** is 0.005 e $Å^{-3}$.

Discussion

In summary, we simultaneously modulated the mesoscale mass transfer and surface reaction active sites of the electrode to achieve highly efficient electrochemical water oxidation process via constructing monodispersed hollow Fe@MoS_2-C sub-micro reactor. Specifically, a group of MoS_2-C hosts with sulfur vacancies and intercalated-carbon were prepared via a micelle-confined microemulsion technology. The FEA results implied that the flow velocity and differential pressure related to mesoscale mass transfer could be highly improved in the hollow nanostructured configuration. The monomolecular carbon was intercalated in the (002) facet of MoS_2 resulting in a superlattice and increasing the number of sulfur vacancies. The sulfur vacancies and intercalated carbon in the hollow host offered a unique microenvironment for Fe anchoring on Mo-Fe-C sites yield the Fe@MoS_2-C sub-micro reactor. Benefitting from the rich mesoscale diffusion and particular local sites, the Fe@MoS_2-C sub-micro reactor delivered a significantly lower OER overpotential than those of the Fe-based SACs reported to data; moreover, it also exhibited excellent stability in continuous electrolysis tests. The operando Raman, XAFS, and HAADF-STEM data revealed the self-reconstruction and catalytic centers. DFT calculations demonstrated the stability of Mo-Fe-C coordination, the electron transfer channel of 'MoO_x → Fe → carbon', and the favorable d-band center in the dual-anchoring model. The kinetics calculations further signified that the dual-anchoring site could change the RDS and optimize the adsorption and desorption of oxygen intermediates, thereby reducing the reaction barriers for water oxidation. Our work involved the simultaneous manipulation of mesoscale mass transfer and highly efficient Mo-Fe-C sites, and might shed light on the design of advanced electrocatalysts through engineering of monodispersed sub-micro reactors.

Methods

Synthesis of MoS_2-C and MoS_2 hosts. The MoS_2-C materials were prepared through a micelle-confined microemulsion technology. Specifically, the water phase solution ($Na_2MoO_4 \cdot 2H_2O$: 1 mmol; glucose: 0.6 g; H_2O: 300 mL) was stepwise added into the oil solution (CTAB: 15 mmol; n-butanol: 100 mL) and strongly stirred for 2 h. 50 mL of ethylene glycol and 0.4 mL of hydrochloric acid were introduced in order and stirred for 5 h. The milky white emulsion was subsequently transferred into a high-pressure autoclave and kept at 220 °C for 24 h. The black powder was produced after the filtration, abstersion (distilled water and absolute ethanol), and drying at 60 °C overnight to obtain the precursor, named as MoS_2-CTAB. The MoS_2-CTAB was treated at 700 °C with 2 °C min^{-1} in Ar for 5 h to produce the hollow MoS_2-C host, named as MoS_2-C. Similarly, the hollow MoS_2 host was synthesized via disposing the MoS_2-CTAB at 850 °C with 10 °C min^{-1} in Ar for 5 h.

Keeping the based conditions constant, a group of MoS_2-C materials with different nanostructured configurations were prepared by changing the amounts of hydrochloric acid to 1.2, 0.8, 0.7, 0.6, 0.5, and 0.3 mL, named as solid MoS_2-C, yolk-shell MoS_2-C-1, yolk-shell MoS_2-C, yolk-shell MoS_2-C-3, hollow MoS_2-C-1, and hollow MoS_2-C-3, respectively.

Synthesis of monodispersed sub-micro reactors. Hollow MoS_2-C hosts (100 mg) were dispersed in a mixed solution (H_2O: 40 mL; ethanol: 20 mL) followed by slowly adding $Fe(NO_3)_3 \cdot 9H_2O$ solution (5 mL, 1 mol L^{-1}). The mixed solution was stirred for 12 h, and the resultant product was separated by centrifugation and dried at 60 °C (vacuum oven) overnight. Finally, the product was treated at 700 °C in Ar for 3 h to obtain the monodispersed hollow Fe@MoS_2-C sub-nano reactor. Similarly, the

Fe@MoS_2 sub-micro reactor was produced by replacing the hollow MoS_2-C with the hollow MoS_2 host.

Accordingly**,** the monodispersed solid Fe@MoS_2-C and yolk–shell Fe@MoS_2-C sub-micro reactors were prepared through changing hollow MoS_2-C host with the solid MoS_2-C and yolk–shell MoS_2-C materials, named as S-Fe@MoS_2-C and Y-Fe@MoS_2-C, respectively.

Characterizations. Powder XRD profiles were identified using a D/max 2550 V diffractometer from 5−65° (λ=1.54056 Å, D8 Advance, Germany). Morphological information was characterized using FESEM (JSM-7001F, Japan) and TEM (JEM-2100, Japan). HAADF-STEM and corresponding EDS mapping analyses were performed on FTEM/STEM (JEM-ARM200F, Japan) with a spherical aberration corrector. Contact angles were measured on a Dataphysics KRUSS apparatus in KOH solution (1 μL, 1M). EPR data was collected using a JES-FA200 (JEOL, Japan). XPS data were collected on a Thermo Scientific Escalab (ESCALAB 250Xi, Massachusetts) with monochromatized Al K_α X-ray source. Raman spectroscopies were conducted using a wavelength of 532 nm on a Raman spectrometer (LabRAM HR Evolution, France). Operando Raman system was built through the combination of the electrochemical workstation (CHI600E, Shanghai), the Raman spectrometer, and the three-electrode pool (C031−1, Gaoss Union). The specific surface areas were obtained by a Belsorp-Mini adsorption apparatus (MicrotracBEL Japan Incorporation, Japan). The pore size distributions were calculated via a BJH method. XAFS data of the Fe K-edge were performed at ANSTO, New South Wales, Australia.

FEA methods. The finite element simulation and analysis (FEA) was performed with the COMSOL Multiphysics, and the corresponding 2D mode was collected. According to the experimental data, the model of the solid sphere was constructed

with a diameter of 540 nm and a pore size of 13 nm; the model of the yolk–shell sphere was plotted with a diameter of 650 nm and a pore diameter of 16 nm; the model of the hollow sphere was constructed with a diameter of 750 nm and a pore diameter of 20 nm. The error of the pore diameter in the models was ±0.2 nm. The calculated domain was simulated via filling water in a rectangular region (6000w nm × 6010h nm). The water was poured from the left boundary, and outflowed from right boundary. The inflow velocity was set to 0.25 m s^{-1} at the entrance. The flow field was done on the "Laminar Flow" module. In order to represent the adhesion of the materials on electrode, the calculated models were all put on the coboundary of the domain in the stationary simulation. The flow field and pressure field were calculated by the Navier-Stokes equations:

$$\nabla \cdot u = 0 \quad (1)$$

$$\rho(u \cdot \nabla)u = \nabla \cdot [-pI + \mu(\nabla u + (\nabla u)^T)] + F \quad (2)$$

Where the u, ρ, p, and F represent the flow velocity, fluid density, pressure, volume force vector, respectively.

Electrochemical measurements. All OER measurements were performed at an electrochemical workstation (CHI600E, Shanghai Chenhua). The working electrodes were prepared by loading the catalyst onto the Ni foam (1×1 cm^2, 0.5 mL, 2 mg mL^{-1}). Then, the nafion-water solution (0.01wt.%, 50 μL of) was evenly dispersed onto the electrodes. The Hg/HgO electrode was used as the reference electrode and the graphite rod was employed as the counter-electrode, respectively. The polarization curves were collected in a 1 M (1 mmol L^{-1}) and 6 M (1 mmol L^{-1}) KOH solution at 5 mV s^{-1}. A reversible hydrogen electrode (RHE) was used to calibrate the potentials, and commercial IrO_2 is tested as the benchmark. The recorded potentials was adjusted by the following equation: $E(\text{vs. RHE}) = E(\text{vs. Hg/HgO}) + (0.098 + 0.0592\text{pH})\ \text{V}$. The overpotential was calculated by the following equation: $\eta = E(\text{vs. RHE}) - 1.23\ \text{V}$. The

C_{dl} of the hollow Fe@MoS_2-C, Fe@MoS_2, MoS_2-C, and MoS_2 catalysts were evaluated via the closed CV data at scanning rates from 20 to 200 mV s^{-1}. The EIS curves were measured at the open-circuit voltages.

Computational details. The DFT calculations was executed in the CASTEP with the generalized gradient approximation (GGA) using the Perdew-Burke-Ernzerhof (PBE) exchange-correlation functional to represent the exchange and correlation effects. Partial sulfur atoms were substituted by oxygen atoms to match with the self-reconstruction. A sulfur atom was removed to represent the sulfur vacancy. The MoS_2 (001) surfaces were modeled by a 3×3 unit cell with two layers of 6.5 Â and the atoms periodically repeated with the vacuum was set 15 Â in z direction. The model that sulfur atoms were substituted by oxygen atoms and removed in MoS_2 cell was named MoO_x. The graphite was modeled by a 4×4 unit cell and inserted into the extended layer of MoO_x with a distance of 9.5 Â forming the MoO_x-C. Fe atoms were putted into the vacancy of sulfur in MoO_x and MoO_x-C to constructing the MoO_x-Fe and MoO_x-Fe-C models. The spin-polarized were added because of the special property of Fe. The k-point and energy cut-off was set to 3×3×1 and 490.0 eV. The self-consistent field, maximal force, maximal stress, and maximal displacement were set to 2.0×10^{-6} eV $atom^{-1}$, 0.05 eV $Â^{-1}$, 0.1GPa, and 0.002 Â. The green and yellow regions in the EDDs mean the electron accumulation and depletion area, respectively.

The adsorption energy (E_{ads}) of the single-atom Fe on the host was computed by the following equation:

$$E_{ads} = E_{Fe@host} - E_{host} - E_{single-atom} \quad (3)$$

where $E_{Fe@host}$, E_{host}, and $E_{single-atom}$ are the total energies of MoO_x, MoO_x-C, MoO_x-Fe, MoO_x-Fe-C, or Fe, respectively.

The bulk cohesive energy (E_{coh}) of the Fe atom on the host was calculated by the

following equation:

$$E_{coh} = E_{bulk}/n - E_{single-atom} \quad (4)$$

where n represents the number of Fe atoms. when $E_{ads} - E_{coh} < 0$ and $E_{ads} < 0$, there is no metal leaching or aggregating, showing that the Fe atoms are stable in the host.

The overall OER process in the alkaline medium involving four electron reaction steps were identified as follows:

$$\text{Step1: } OH^- + * \rightarrow OH^* + e^- \quad (5)$$

$$\text{Step2: } OH^* + OH^- \rightarrow O^* + H_2O\,(l) + e^- \quad (6)$$

$$\text{Step3: } O^* + OH^- \rightarrow OOH^* + e^- \quad (7)$$

$$\text{Step4: } OOH^* + OH^- \rightarrow O_2\,(g) + H_2O\,(l) + e^- + * \quad (8)$$

and the Gibbs free energy change (ΔG) for each step was calculated by the following equation:

$$\Delta G1 = E_{DFT}^{OH^*} - E_{DFT}^{*} + \frac{1}{2}E_{DFT}^{H_2(g)} - E_{DFT}^{H_2O(l)} + \Delta ZPE - T\Delta S \quad (9)$$

$$\Delta G2 = E_{DFT}^{O^*} - E_{DFT}^{OH^*} + \frac{1}{2}E_{DFT}^{H_2(g)} + \Delta ZPE - T\Delta S \quad (10)$$

$$\Delta G3 = E_{DFT}^{OOH^*} - E_{DFT}^{O^*} + \frac{1}{2}E_{DFT}^{H_2(g)} - E_{DFT}^{H_2O(l)} + \Delta ZPE - T\Delta S \quad (11)$$

$$\Delta G4 = E_{DFT}^{*} - E_{DFT}^{OOH^*} + 2E_{DFT}^{H_2O(l)} - \frac{3}{2}E_{DFT}^{H_2(g)} + 4.92 + \Delta ZPE - T\Delta S \quad (12)$$

Where the E_{DFT}^{*}, $E_{DFT}^{O^*}$, $E_{DFT}^{OH^*}$, $E_{DFT}^{OOH^*}$, $E_{DFT}^{H_2(g)}$, and $E_{DFT}^{H_2O(l)}$ are the total energies of the catalyst, O*, OH*, and OOH* adsorbed on catalyst surface, H_2, and H_2O molecule obtained from DFT calculation. ΔZPE and ΔS are the change in zero point energies and entropy at 298 K (T). The theoretical overpotential (η) is calculated by the following equation:

$$\eta = -\min(\Delta G1, \Delta G2, \Delta G3, \Delta G4) \quad (13)$$

References

1. Staffell I. et al. The role of hydrogen and fuel cells in the global energy system. *Energ. Environ. Sci.* **12**, 463-491 (2019).

2. Liu S. et al. Turning main-group element magnesium into a highly active electrocatalyst for oxygen reduction reaction. *Nat. Commun.* **11**, 938 (2020).
3. Pang Y., Su C., Jia G., Xu L. & Shao Z. Emerging two-dimensional nanomaterials for electrochemical nitrogen reduction. *Chem. Soc. Rev.*, Doi: 10.1039/d1cs00120e, (2021).
4. Zhou H. et al. Engineering the Cu/Mo_2CT_x (MXene) interface to drive CO2 hydrogenation to methanol. *Nat. Catal.* **4**, 860-871 (2021).
5. Chen F.-Y., Wu Z.-Y., Adler Z. & Wang H. Stability challenges of electrocatalytic oxygen evolution reaction: From mechanistic understanding to reactor design. *Joule*, **5**, 1704-1731 (2021).
6. Montoya J. H. et al. Materials for solar fuels and chemicals. *Nat. Mater.* **16**, 70-81 (2016).
7. Yu F. et al. High-performance bifunctional porous non-noble metal phosphide catalyst for overall water splitting. *Nat. Commun.* **9**, 2551 (2018).
8. Jiang K. et al. Dynamic active-site generation of atomic iridium stabilized on nanoporous metal phosphides for water oxidation. *Nat. Commun.* **11**, 2701 (2020).
9. Kweon D. H. et al. Ruthenium anchored on carbon nanotube electrocatalyst for hydrogen production with enhanced Faradaic efficiency. *Nat. Commun.* **11**, 1278 (2020).
10. Oh N. K. et al. Highly efficient and robust noble-metal free bifunctional water electrolysis catalyst achieved via complementary charge transfer. *Nat. Commun.* **12**, 4606 (2021).
11. Hong W. T. et al. Toward the rational design of non-precious transition metal oxides for oxygen electrocatalysis. *Energ. Environ. Sci.* **8**, 1404-1427 (2015).
12. Chen Q.-X. et al. Microchemical engineering in a 3D ordered channel enhances electrocatalysis. *J. Am. Chem. Soc.* **143**, 12600-12608 (2021).
13. Jing L. et al. Mesoscale diffusion enhancement of carbon-bowl-shaped nanoreactor toward high-performance electrochemical H_2O_2 production. *ACS Appl. Mater. Interfaces* **13**, 39763-39771 (2021).
14. Costentin C., Di Giovanni C., Giraud M., Savéant J.-M. & Tard C. Nanodiffusion in electrocatalytic films. *Nat. Mater.* **16**, 1016-1021 (2017).
15. Tang C., Wang H.-F. & Zhang Q. Multiscale principles to boost reactivity in gas-involving energy electrocatalysis. *Acc. Chem. Res.* **51**, 881-889 (2018).
16. Smith C. P. & Dwhite H. S. Theory of the interfacial potential distribution and reversible voltammetric response of electrodes coated with electroactive molecular films. *Anal. Chem.* **64**, 2398-2405 (1992).
17. Zhang Q. et al. Highly efficient electrosynthesis of hydrogen peroxide on a superhydrophobic three-phase interface by natural air diffusion. *Nat. Commun.* **11**, 1731 (2020).
18. Xia C. et al. Confined local oxygen gas promotes electrochemical water oxidation to hydrogen peroxide. *Nat. Catal.* **3**, 125-134 (2020).
19. He R., Chen S., Yang F. & Wu B. Dynamic diffuse double-layer model for the electrochemistry of nanometer-sized electrodes. *J. Phys. Chem. B* **110**, 3262-3270 (2006).
20. Jaramillo T. F. et al. Identification of active edge sites for electrochemical H_2 evolution from MoS_2 nanocatalysts. *Science* **317**, 100-102 (2007).
21. Xie J. et al. Controllable disorder engineering in oxygen-incorporated MoS_2 ultrathin nanosheets for efficient hydrogen evolution. *J. Am. Chem. Soc.* **135**, 17881-17888 (2013).
22. Zhang P. et al. Chemically activated MoS_2 for efficient hydrogen production. *Nano Energy* **57**, 535-541 (2019).
23. Zhang G., Liu H., Qu J. & Li J. Two-dimensional layered MoS_2: rational design, properties and electrochemical applications. *Energ. Environ. Sci.* **9**, 1190-1209 (2016).
24. Huang K. et al. Hollow-structured metal oxides as oxygen-related catalysts. *Adv. Mater.* **31**, e1801430 (2019).
25. Li Y. et al. High-valence nickel single-atom catalysts coordinated to oxygen sites for extraordinarily activating oxygen evolution reaction. *Adv. Sci.* **7**, 1903089 (2020).

26. Ji X. et al. Graphene/MoS_2/$FeCoNi(OH)_x$ and graphene/MoS_2/$FeCoNiP_x$ multilayer-stacked vertical nanosheets on carbon fibers for highly efficient overall water splitting. *Nat. Commun.* **12**, 1380 (2021).
27. Fan L. Z. et al. 3D core-shell NiFeCr catalyst on a Cu nanoarray for water oxidation: synergy between structural and electronic modulation. *ACS Energy Lett.* **3**, 2865-2874 (2018).
28. Deng S. et al. Synergistic doping and intercalation: realizing deep phase modulation on MoS_2 arrays for high-efficiency hydrogen evolution reaction. *Angew. Chem. Int. Ed.* **58**, 16289-16296 (2019).
29. Wu Y.-L. et al. Ordered macroporous superstructure of nitrogen-doped nanoporous carbon implanted with ultrafine Ru nanoclusters for efficient pH-universal hydrogen evolution reaction. *Adv. Mater.* **33**, 2006965 (2021).
30. Hu H., Han L., Yu M., Wang Z. & Lou X. W. Metal–organic-framework-engaged formation of Co nanoparticle-embedded carbon@Co_9S_8 double-shelled nanocages for efficient oxygen reduction. *Energ. Environ. Sci.* **9**, 107-111 (2016).
31. Prieto G. et al. Hollow nano- and microstructures as catalysts. *Chem. Rev.* **116**, 14056-14119 (2016).
32. Gong F. et al. Boosting electrochemical oxygen evolution over yolk-shell structured O–MoS_2 nanoreactors with sulfur vacancy and decorated Pt nanoparticles. *Nano Energy* **78**, 105284 (2020).
33. Gong F. et al. All-pH stable sandwich-structured MoO_2/MoS_2/C hollow nanoreactors for enhanced electrochemical hydrogen evolution. *Adv. Funct. Mater.* **31**, 2101715 (2021).
34. Zhang J. et al. Designed formation of double-shelled Ni-Fe layered-double-hydroxide nanocages for efficient oxygen evolution reaction. *Adv. Mater.* **32**, e1906432 (2020).
35. Mefford J. T. et al. Correlative operando microscopy of oxygen evolution electrocatalysts. *Nature* **593**, 67-73 (2021).
36. Wu Z. P. et al. Manipulating the local coordination and electronic structures for efficient electrocatalytic oxygen evolution. *Adv. Mater.*, **33** e2103004 (2021).
37. Bai L., Hsu C.-S., Alexander D. T. L., Chen H. M. & Hu X. Double-atom catalysts as a molecular platform for heterogeneous oxygen evolution electrocatalysis. *Nat. Energy*, **13**, 3594 (2021).
38. Hulva J. et al. Unraveling CO adsorption on model single-atom catalysts. *Science* **371**, 375-379 (2021).
39. Qiao B. et al. Single-atom catalysis of CO oxidation using Pt_1/FeO_x. *Nat. Chem.* **3**, 634-641 (2011).
40. Guo X. et al. Direct, Nonoxidative conversion of methane to ethylene, aromatics, and hydrogen. *Science* **344**, 616-619 (2014).
41. Sun T. et al. Engineering of coordination environment and multiscale structure in single-site copper catalyst for superior electrocatalytic oxygen reduction. *Nano Lett.* **20**, 6206-6214 (2020).
42. Yang H. et al. A universal ligand mediated method for large scale synthesis of transition metal single atom catalysts. *Nat. Commun.* **10**, 4585 (2019).
43. Hu S. & Li W.-X. Sabatier principle of metal-support interaction for design of ultrastable metal nanocatalysts. *Science,* eabi9828 (2021).
44. Primbs M. et al. Establishing reactivity descriptors for platinum group metal (PGM)-free Fe–N–C catalysts for PEM fuel cells. *Energ. Environ. Sci.* **13**, 2480-2500 (2020).
45. Luo F. et al. P-block single-metal-site tin/nitrogen-doped carbon fuel cell cathode catalyst for oxygen reduction reaction. *Nat. Mater.* **19**, 1215-1223 (2020).
46. Kuang P. et al. Pt single atoms supported on N-doped mesoporous hollow carbon spheres with enhanced electrocatalytic H_2 evolution activity. *Adv. Mater.* **33**, 2008599 (2021).
47. Zhang Y. et al. Engineering oversaturated Fe-N_5 multi-functional catalytic sites for durable lithium-sulfur batteries. *Angew. Chem. Int. Ed.* **60**, 2-10 (2021).
48. Singh B. et al. Single-atom (iron-based) catalysts: synthesis and applications. *Chem. Rev.* **121**, 13620-13697 (2021).

49. Lang R. et al. Single-atom catalysts based on the metal–oxide interaction. *Chem. Rev.* **120**, 11986-12043 (2020).
50. Zheng J. et al. High loading of transition metal single atoms on chalcogenide catalysts. *J. Am. Chem. Soc.* **143**, 7979-7990 (2021).
51. Zhai P. et al. Engineering single-atomic ruthenium catalytic sites on defective nickel-iron layered double hydroxide for overall water splitting. *Nat. Commun.* **12**, 4587 (2021).
52. Yu L., Deng D. & Bao X. Chain mail for catalysts. *Angew. Chem. Int. Ed.* **59**, 15294-15297 (2020).
53. Zheng X. B. et al. Non-carbon-supported single-atom site catalysts for electrocatalysis. *Energ. Environ. Sci.* **14**, 2809-2858 (2021).
54. Wang X. et al. Single-atom vacancy defect to trigger high-efficiency hydrogen evolution of MoS_2. *J. Am. Chem. Soc.* **142**, 4298-4308 (2020).
55. Hu J. et al. Sulfur vacancy-rich MoS_2 as a catalyst for the hydrogenation of CO_2 to methanol. *Nat. Catal.* **4**, 242-250 (2021).
56. Park S. et al. Enhancing catalytic activity of MoS_2 basal plane S-vacancy by Co cluster addition. *ACS Energy Lett.* **3**, 2685-2693 (2018).
57. Ge J. et al. Dual-metallic single Ru and Ni atoms decoration of MoS_2 for high-efficiency hydrogen production. *Appl. Catal. B: Environm.***298**, 120557 (2021).
58. Zhu J. et al. Boundary activated hydrogen evolution reaction on monolayer MoS_2. *Nat. Commun.* **10**, 1348 (2019).
59. Xu Q. et al. Atomic heterointerface engineering breaks aActivity limitation of electrocatalysts and promises highly-efficient alkaline water splitting. *Energ. Environ. Sci.* **14**, 5228-5259 (2021).
60. Tian H., Liang J. & Liu J. Nanoengineering carbon spheres as nanoreactors for sustainable energy applications. *Adv. Mater.* **31**, e1903886 (2019).
61. Liu J. et al. Yolk-shell hybrid materials with a periodic mesoporous organosilica shell: ideal nanoreactors for selective alcohol oxidation. *Adv. Funct. Mater.* **22**, 591-599 (2012).
62. Boyjoo Y. et al. Engineering nanoreactors for metal-chalcogen batteries. *Energ. Environ. Sci.* **14**, 540-575 (2021).
63. Li T. et al. Self-assembled nanoparticle supertubes as robust platform for revealing long-term, multiscale lithiation evolution. *Matter* **1**, 976-987 (2019).
64. Ding H., Liu H., Chu W., Wu C. & Xie Y. Structural transformation of heterogeneous materials for electrocatalytic oxygen evolution reaction. *Chem. Rev.* **121**, 13174-13212 (2021).
65. Xu H. X., Cheng D. J., Cao D. P. & Zeng X. C. A universal principle for a rational design of single-atom electrocatalysts. *Nat. Catal.* **1**, 339-348 (2018).
66. Miao Z. et al. Improving the stability of non-noble-metal M-N-C catalysts for proton-exchange-membrane fuel cells through M-N bond length and coordination regulation. *Adv. Mater.* **33**, 2006613 (2021).

Acknowledgements

F.L.G. and M.L. contributed equally to this work. The authors thank funds from National Natural Science Foundation of China (NSFC: 52002359, 21902157, and U1704256), the Dalian National Laboratory for Clean Energy (DNL), CAS, DNL Cooperation Fund, CAS (DNL180402), Zhengzhou University of Light Industry (2020ZCKJ203 and 2018BSJJ027). We also gratefully acknowledge National Supercomputing Center in Zhengzhou, P. R. China for providing the computational

nodes, and thanks Dr. Chen Zhao for the contact angles experiment and the analysis.

Authors Contributions

F.L.G. prepared the materials, analyzed the data, conceived the project, and wrote the manuscript. M.L. did most of the experimental work, performed most characterizations, and analyzed the data. L.H.G. carried out the theoretical calculations, analyzed the data, and plotted the Figures. S.Y. proposed the original concept and discussed the results. Q.K.J. conducted the HAADF experiments and analysis. G.Z. contributed the EPR and the analysis. X.L.Z. analyzed the data and discussed the results. Z.K.P. were involved the TEM and EDS mapping characterizations. Y.H.Z contributed the explanations of the DFT. S.M.F. discussed the studies, revised and edited the manuscript. J.L. conceived the original concept, discussed the results, and edited the manuscript.

Conflicting Interest

The authors declare no competing interests.

Supplementary Files

This is a list of supplementary files associated with this preprint. Click to download.

- Supplementaryinformation.doc